APPLIED PHYSICS

A tunable metamaterial microwave absorber inspired by chameleon's color-changing mechanism

Dahyun D. Lim[1], Alberto Ibarra[1], Jeongwoo Lee[2], Jiyoung Jung[1], Wonjoon Choi[2], Grace X. Gu[1]*

A metamaterial absorber capable of swiftly altering its electromagnetic response in the microwave range offers adaptability to changing environments, such as tunable stealth capabilities. Inspired by the chameleon's ability to change color through the structural transformation of photonic lattice crystals, which shift the bandgaps of reflection and transmission of visible light, we designed a crisscross structure that transforms from an expanded to a collapsed form. This transformation enables a switch between broadband absorption and peak transmission in the microwave range (4 to 18 gigahertz). The structure, optimized through data-driven design, is mechanically actuated by the rotation of interlinked trusses. This mechanism changes the entire array's response, allowing it to remain undetected by an external radar or to transmit an internal radar signal to a near-field receiver when needed. The mechanical actuation and the shifting electromagnetic response of the arrayed structure are demonstrated.

INTRODUCTION

As the application of electromagnetic waves in the microwave range, such as wireless communication or defense radar increases, the need for effective attenuation of these waves becomes increasingly critical to reduce electromagnetic wave pollution and interference or stealth capability to remain undetected by the radar (*1*–*3*). Among electromagnetic response of reflection, transmission, and absorption, controlling absorption is the most challenging as it requires reducing both reflection and transmission through impedance matching and dissipating the incoming wave into other forms of energy, such as heat (*4*). A straightforward way to achieve attenuation is by using radar-absorbing materials, for instance, carbon-based dielectric lossy materials or ferrite-based magnetic lossy materials with high dissipation properties (*5*–*7*). However, solely controlling electromagnetic properties (permittivity and permeability) through the material limits its effective attenuation (e.g., broadband absorption) as the structural absorption is overlooked. Thus, a metamaterial absorber was introduced, which successfully improved attenuation by introducing engineered architecture (*8*, *9*). These metamaterial absorbers include periodically arranged metallic patterns, change of dielectric layers, and three-dimensional (3D) unit cell structures (*10*, *11*). 3D unit cell structures achieve broadband absorption in multiple bandwidths through increased impedance matching and multiple reflection and scattering inside geometries such as honeycomb (*12*), lattices (*13*–*15*), or periodic minimal surface structures (*16*).

The advancement in additive manufacturing combined with a lossy material led to implementation of diverse 3D structures as structural absorbers, removing the constraints of fabricating complex geometries (*17*–*20*). These 3D unit cells include octet-truss (*14*, *15*, *21*), gyroid (*16*), and kelvin foam (*13*) toward the broadband absorbers within lightweight and robust structures enabling multiple bandwidths attenuating more than 90% of the incoming waves. The engineered porosity of the unit cells improves impedance matching, reducing the reflection, and the internal structure, composed of multiple angled struts or surfaces, leads to scattering and multiple reflections, increasing dissipation as the waves transmit through the structure. This structural approach using 3D geometry notably adds more parameters to adjust the electromagnetic response compared to only relying on the material's inherent properties. However, a major limitation of these structural absorbers is their fixed electromagnetic response after fabrication—a single electromagnetic response from a single design.

In real-world scenarios, a tunable electromagnetic response from a single design is expected for structural absorbers to adapt to the dynamic changes in the bandwidth of incoming waves or to control outgoing signals (*8*, *22*). Hence, several strategies were previously used to introduce tunability to the structural absorber: changing the electrical properties of periodic circuit patterns (*23*), tuning permittivity or permeability by varying the thickness of the dielectric spacer (*24*), and transforming the 3D structure through mechanical transformation such as origami (*25*). Among them, mechanical transformation of 3D structure has a competitive advantage in achieving broadband absorption through structural absorption and reduced interference from the use of additional electrical components (*22*). Despite the promise of mechanically transformed structural absorber, prior works focused on demonstrating changes in strength or bandwidth in absorption, rather than targeting specific electromagnetic response. In addition, the actuation method to control the transformation of the structure is often overlooked. For example, the origami design and actuation introduce the tunability of the response, but precisely changing the angle of the origami planes for unit cells must be changed individually. Thus, a new tunable structural absorber that is programmable to the targeted electromagnetic response and can transform through mechanical actuation continuously is required. However, as introducing structural transformation increases the possible geometries that affect electromagnetic response, using a trial-and-error method through experiments is challenging to configure an optimal structure.

In this study, we introduce a tunable structural absorber that can continuously vary electromagnetic response from absorption to transmission in the microwave range across three bandwidth (4 to 18 GHz, including X, Ku, and C bands). The tunable structural absorber is inspired by how chameleons vary their electromagnetic response in the visible light range. Chameleons change color through structural transformation by rearranging lattices formed with photonic crystals,

[1]Department of Mechanical Engineering, University of California, Berkeley, CA 94720, USA. [2]School of Mechanical Engineering, Korea University, Seoul, 02841, Republic of Korea.
*Corresponding author. Email: ggu@berkeley.edu

which results in changes of transmission and reflection in visible wavelengths (*26*). Using the same tuning mechanism, a designed crisscross structure varies the electromagnetic response in the microwave range from broadband absorption to transmission mode by transforming its structure from a collapsed to an expanded form. By changing the angle between dielectric lossy material–based trusses, the transmission and absorption of the incoming microwave change due to the altered spacing and angles between interlinked trusses. This phenomenon is analogous to a chameleon's structural transformation, where it changes the spacing between photonic crystals to modulate light reflection. To ensure rationally yet effectively optimizing the structure for target functions, a data-driven design approach including a machine learning–based surrogate model trained with results of finite element analysis (FEA) and optimization through a genetic algorithm is presented. The optimized structures are validated through experiments from assembled structure that successfully switches between more than 90% absorption in the entire measured frequency range (5.85 to 18 GHz) in a collapsed form and a peak transmission of 24.2% when expanded. In addition, the transformation of the entire array through mechanical actuation is demonstrated with synchronized movement derived from a crisscross linkage system. The presented design overcomes the challenge of tunable structural absorbers with programmability and simultaneous actuation.

RESULTS

Tunable structure inspired by chameleon

Figure 1A shows a tunable crisscross unit cell structure proposed in this study. It is assembled with dielectric lossy material–based trusses and polymer-based connectors and hinges for the connection. The truss part, made of carbon black and polylactic acid composites (CB/PLA), primarily determines the electromagnetic response of the structure, because the dielectric lossy property of the material interacts with incoming electromagnetic wave through attenuation and reflection. On the other hand, hinges made from polycarbonate and connectors fabricated with photocurable polymers (VeroWhite and TangoBlack Plus) have minimal influence on the incoming waves due to the low electrical conductivity and low dielectric loss tangent (*27*, *28*). The main objectives of these hinges and connectors are to assist the mechanical assembly and actuation of the arrayed structure without affecting the electromagnetic response. The unit cell structure is inspired by how panther chameleons rapidly change their skin colors (*26*). While many other animals like cephalopods change color primarily through a pigment-based mechanism (*29*), chameleons change color through structural transformation of the guanine nanocrystals inside their skin layers. By actively tuning the spacing between these nanocrystals, with a lattice constant close to the incident wavelength, the photonic bandgap shifts, resulting in

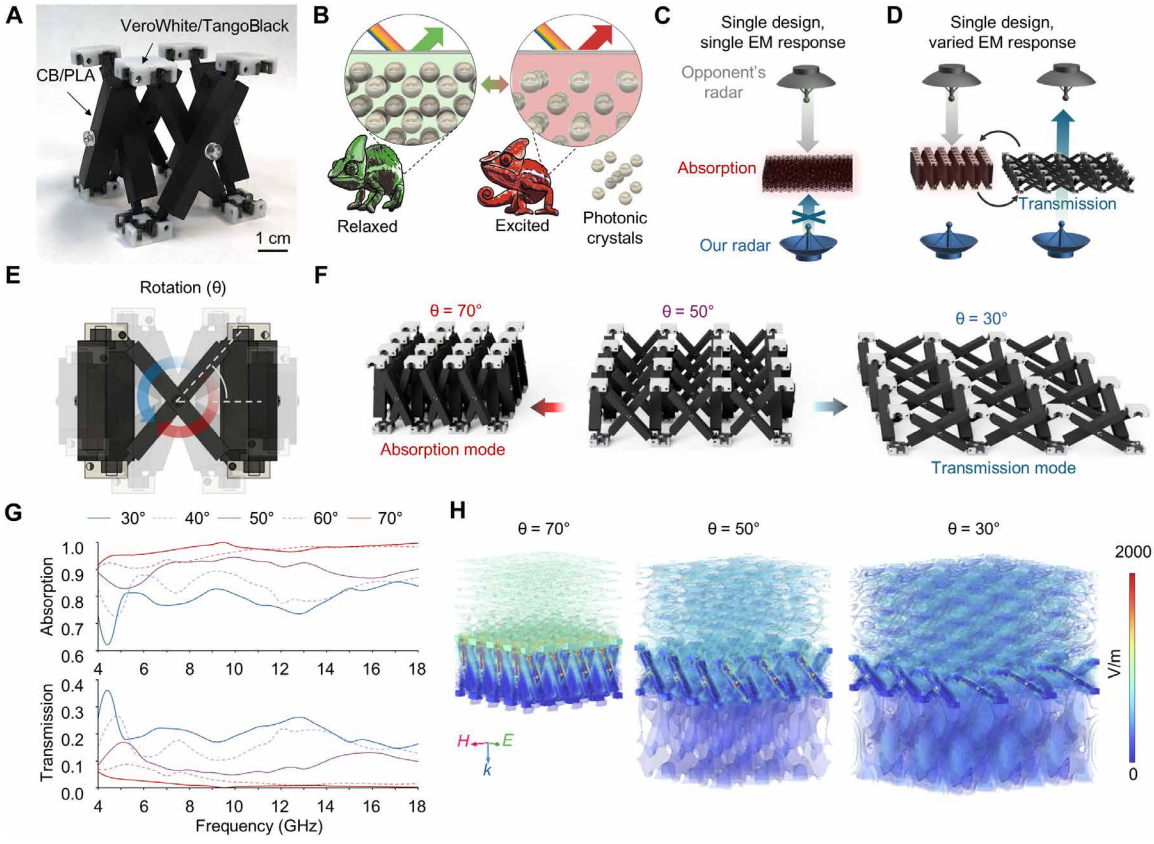

Fig. 1. Comprehensive overview of the tunable crisscross design. (**A**) A photograph of the unit cell structure of the crisscross design with a scale bar of 1 cm. (**B**) A schematic of chameleon's color change from green to red by tuning reflection in visible light through adjusting the spacing between photonic crystals. (**C**) A schematic illustration of a structural broadband microwave absorber without tunability and (**D**) the proposed tunable crisscross structure that changes between absorption and transmission electromagnetic (EM) response modes. (**E**) Mechanical actuation of the structure through rotation. (**F**) Renders of the assembled crisscross structure when shifting from 70° (absorption mode) to 30° (transmission mode). (**G**) Absorption and transmission of the tunable structure varying from 30° to 70° calculated using FEA. (**H**) Electric field of the structure with isosurface and 3D volumetric views of the crisscross structure in 30°, 50°, and 70° at 8 GHz.

changes in transmission and reflection intensity in the visible (240 to 480 nm) and near-infrared spectrum (700 to 1400 nm) (Fig. 1B). On the basis of these findings, we hypothesize that changing the lattice structure of the tunable unit cell, with a lattice constant of the centimeter scale, can manipulate the electromagnetic response in the centimeter-scale incident wavelength microwave bandwidth (4 to 18 GHz), which is approximately five orders of magnitude different from the wavelength of visible light.

As depicted in Fig. 1C, the objective of the tunable absorbing structure is to overcome the limitation of fixed electromagnetic response in previously proposed structural broadband absorbers. Structural broadband absorbers have proven to be beneficial in increasing the attenuation of the baseline material property by incorporating geometrical features (e.g., porosity, facet, or strut-based architecture). The engineered porosity of a structural absorber from the lattice enables impedance matching with free space and increased absorption through multiple internal scattering, reflection, and resonances. However, the electromagnetic response of the broadband absorber cannot be tuned once it is fabricated. This leaves a single structure tied to a single electromagnetic response. While it is advantageous to absorb unwanted signals, the fixed electromagnetic properties of the structure cannot perform the switchable function between the absorption and transmission. For example, shielding an object inside the broadband absorber from the external radar is possible, but it is also impossible to transmit the signal from an internal radar to outside for detection.

In comparison, the proposed tunable structure swiftly varies the electromagnetic response with a single structure (Fig. 1D). By changing the angle of rotation (θ) between crisscross trusses, electromagnetic response changes from broadband absorption mode to transmission mode. Figure 1E depicts a side view of the unit cell geometry, in which the structure can continuously change its spacing between trusses by rotating revolute joints at the hinge and connectors. Interlinked crisscross trusses with hinges and connectors enable synchronized movement of the whole structure from the movement of a single unit cell structure. This mechanism enables the rotation of a single truss to lead to the transformation of the entire array, as shown in Fig. 1F. The mechanical design of truss, connectors and synchronized actuation is inspired by Hoberman sphere, a deployable interlinked spherical toy, as described in fig. S1.

This tunable structure can perform as a broadband structural absorber, with more than 90% absorption across the entire frequency range of 4 to 18 GHz and nearly zero transmission in the collapsed form ($\theta = 70°$ in Fig. 1G). When the interlinked crisscross rotates and expands, the structure can transmit more than 30% at 4.5 GHz at $\theta = 30°$. This peak transmission can be used for wireless communication to the outside when necessary, such as for emergency communication or data transmission. Figure 1H plots the isosurface of electric field distribution at 8 GHz, highlighting the change in electromagnetic responses. The electromagnetic wave is primarily dissipated between the truss structures when collapsed ($\theta = 70°$) with minimal transmission of the electric field below the structure. However, as the gaps increase with rotation, θ changes to 50° and 30°, and the incoming waves begin to pass through the structure. The detailed design, optimization, fabrication, and experiments of the proposed tunable structure will be presented in the following sections.

Data-driven design of tunable structural absorber

The performance of the tunable structure in terms of transmission, absorption, and reflection is governed by the material properties and geometry of the unit cell components. While the electromagnetic properties of the material are unmodifiable after fabrication, structural absorbers can tune electromagnetic response by changing geometric parameters of the unit cell structure. For example, varying the geometric parameter of mechanical metamaterials (octet-truss, octet-foam, or kelvin foam) fabricated with equal porosity of CB/PLA composites results in variance in the absorption, transmission, and reflection of the incoming wave (*13*–*15*). Thus, exploring the effect of geometric parameters in tunable structures on the electromagnetic response is necessary. However, even with the basic crisscross design modeled out of boxes and cylinders as presented in Fig. 1A, an infinite number of unit cell designs can be generated by changing the dimensions of the geometric features. This vast number of geometries makes programming of the tunable structure toward objectives challenging. A potential solution to overcoming the challenge of exploring possible geometries of metamaterials is to use a machine learning–driven approach, such as inverse design and reinforcement learning, to efficiently explore complex design spaces (*30*–*34*). Thus, rather than arbitrarily selecting the design parameters based on trial and error, we choose a data-driven design approach using FEA, neural networks, and genetic algorithms to predict and optimize the tunable structure toward the target function. The goal is to efficiently explore the optimized structures for specific electromagnetic responses such as broadband absorption or high transmission at certain frequencies, enabling rapid selection of tunable unit cell designs. While the complexity of the unit cell design can exponentially increase by adding additional geometric parameters (e.g., fillets, draft angles, and holes on trusses), our design is simplified into a total of five significant input variables: truss length (l), truss width (w), truss thickness (t), rotational angles (θ), and incident electromagnetic wave frequency (f) as described in Fig. 2A. By varying the input variables, the electromagnetic response, the absorption, reflection, and transmission are considered as outputs.

FEA can effectively simulate the electromagnetic response of structural absorbers fabricated with CB/PLA composites (*13*, *15*, *21*). However, as FEA often requires heavy computing resources to obtain outputs, the optimization process can be expedited by using machine learning–based surrogate models (*35*–*38*). Thus, to acquire training datasets for machine learning models, the electromagnetic response of 5000 datasets with randomly generated input parameters are simulated. Input variables are randomly generated under the following conditions, where the dimension is described in the format of "minimum to maximum": truss length in 25 to 60 mm, truss width in 4 to 6 mm, truss thickness in 4 to (truss length × 0.16) mm, rotational angle in 25° to 75°, and incident frequency in 4 to 12 GHz. These dimensions are set considering the manufacturing constraints and minimizing the computing resources required for the simulation. For instance, angles exceeding 75° can cause structural overlap depending on the randomly generated truss dimensions. Power loss density plots in Fig. 2B present examples of the simulated results with varying inputs. The material properties used in the simulation are permittivity and permeability values of CB/PLA composites, and pristine polylactic acid is used for simulation (*15*).

Figure 2C describes the correlation matrix of five inputs and three outputs from the FEA results to elucidate the correlation coefficients between variables. Three inputs (incident frequency, truss thickness, and rotational angle) present meaningful correlations with transmission and absorption. Incident frequency has a moderate negative correlation with transmission (−0.34) and a positive

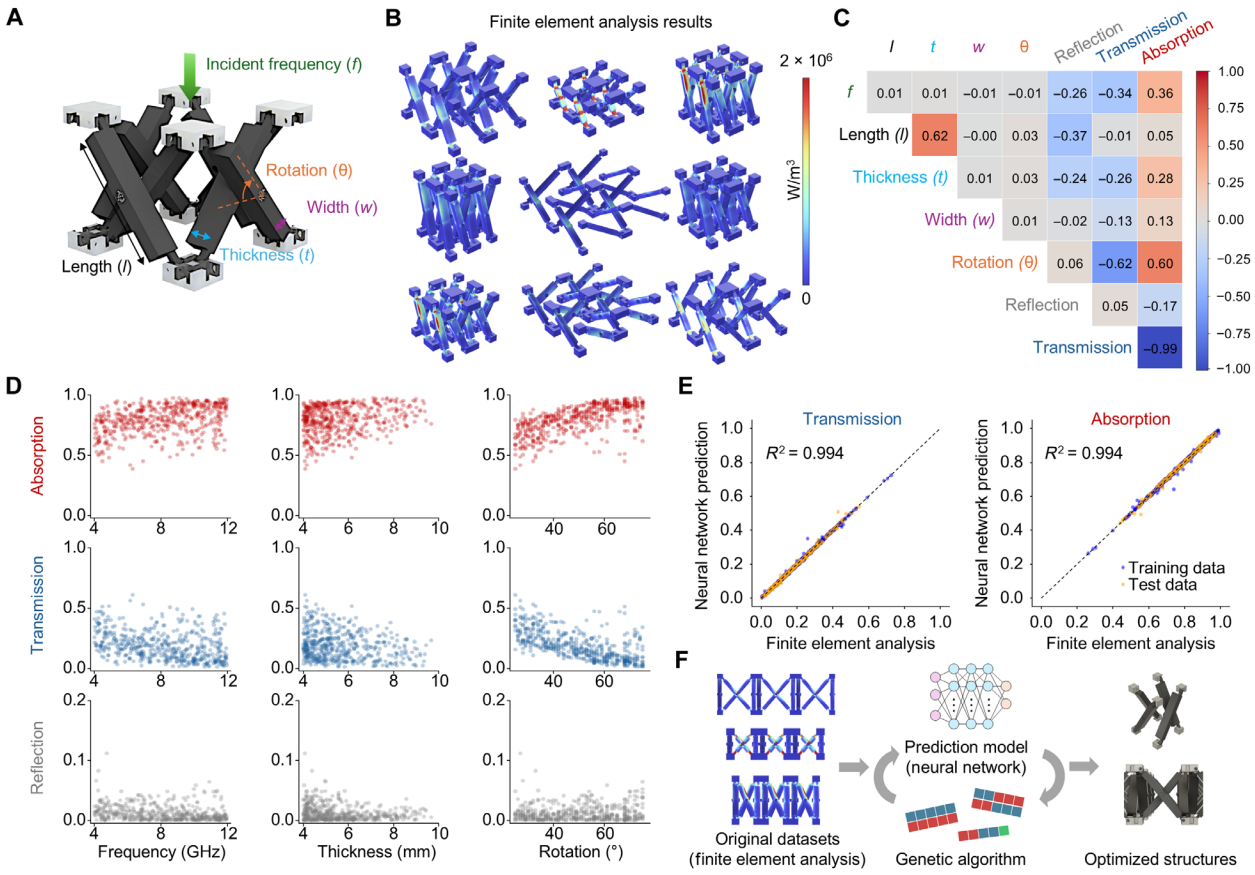

Fig. 2. Data-driven design of the tunable structure. (**A**) Five input variables for data generation: incident frequency (*f*), rotational angle (θ), truss thickness (*t*), truss width (*w*), and truss length (*l*). (**B**) Examples of FEA results with power loss density plots. (**C**) Correlation matrix of five inputs and three outputs: reflection, transmission, and absorption. (**D**) Plots comparing frequency, truss thickness, and rotational angle (inputs) to absorption, transmission, and reflection (outputs). (**E**) Prediction (neural network) to FEA comparison on transmission and absorption. (**F**) Diagram of the prediction and the optimization process with the neural network and the genetic algorithm.

correlation with absorption (0.36). Similarly, truss thickness exhibits a moderate negative correlation with transmission (−0.26) and a positive correlation with absorption (0.28). Last, a rotational angle displays the strongest positive correlation with absorption (0.60) and a negative correlation with transmission (−0.62). Scatterplots in Fig. 2D visualize these correlations, where the general trend indicates that increased frequency, truss thickness, and rotational angle result in increased absorption and decreased transmission. However, a limited linear relationship exists between inputs and outputs, as many outlier data points exist. This is due to the slight change in structural features causing variance in electromagnetic response due to internal scattering, reflection, or resonances. The comparison of prediction models fitted with linear and polynomial regression supports this interpretation. When 5000 FEA results are divided into 80% training set and 20% test sets, a prediction model using linear regression or polynomial regression (with degrees from 2 to 5) predicts the absorption and transmission with an R^2 value of less than 0.90 (table S1). Compared to linear or polynomial regression models, the neural network provides more accurate predictions, with R^2 of 0.994 for both absorption and transmission (Fig. 2E). In addition to the improved accuracy, the neural network–based surrogate model predicts the electromagnetic response multiple orders of magnitude faster than FEA. For example, a randomly chosen case among 5000 datasets, the FEA-based simulation takes 64 s, whereas it takes only 12 ms for the neural network prediction model with only a 0.3% difference in predicted electromagnetic response (table S2). Thus, the generated prediction model through the neural network will be an effective surrogate model for the optimization process as described in the flow diagram (Fig. 2F).

Optimization of tunable structure with varying electromagnetic response

Using the neural network–based surrogate model, an optimized tunable structure for broadband absorption is determined through a genetic algorithm. The optimization goal is to achieve broadband absorption more than 90% across the entire bandwidth (Fig. 3A). By applying a genetic algorithm described in Materials and Methods, the following variables are extracted that meet the optimization goal: truss length of 58.4 mm, thickness of 9.60 mm, width of 5.90 mm, and rotational angle of 66.9° (Fig. 3A). Figure 3B presents the optimized structure with the identified crisscross truss dimensions shifting from the collapsed to the expanded form. A total of 81 absorption values from 4.0 to 12.0 GHz with a 0.1-GHz step size are calculated using the surrogate model. The optimized structure achieves broadband absorption with a minimum of 92.3% at 4.0 GHz, a maximum of 99.2% at 8.8 GHz, and an average absorption of

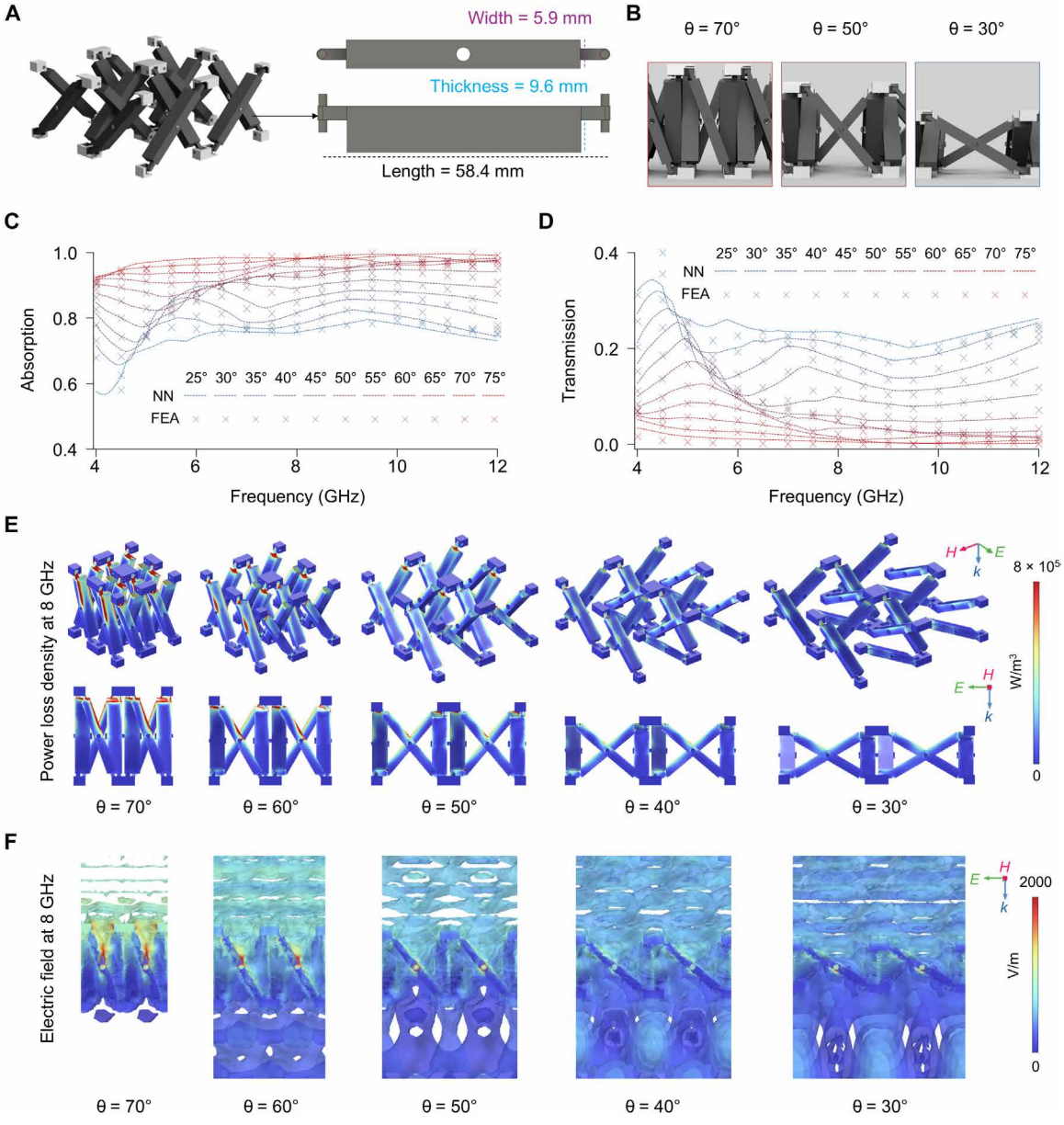

Fig. 3. Representative designs of optimized structures for broadband absorption. (**A**) Render of design optimized for broadband absorption with dimensional information of the truss. (**B**) Actuation of the optimized structure at 70°, 50°, and 30°. Comparison of FEA (scatterplot with "×" marker) and neural network (NN) simulation results (dashed line) in (**C**) absorption and (**D**) transmission when rotation varies from 25° to 75°. (**E**) Power loss density plot and (**F**) 3D isosurface electric field plots of the structure with varying rotational angles at 8 GHz.

96.4% throughout the 4- to 12-GHz range. Optimizing for broadband absorption is straightforward, as the correlation matrix analysis indicated steeper angle and thicker truss result in higher absorption, while longer truss length reduces reflection.

While fixing the truss dimensions (length, thickness, and width), the tunable electromagnetic response is demonstrated by changing the angle from 25° (blue dashed line) to 75° (red dashed line) with a 5° step size in Fig. 3 (C and D). As the structure transforms from the collapsed (75°) to the expanded form (25°), the electromagnetic response shifts from broadband absorption mode to transmission mode. To validate the accuracy of the surrogate model and analyze the absorbing mechanism, finite element results are cross-checked using identical input variables. The calculated absorption and transmission values from the analysis are marked with "×" in Fig. 3 (C and D).

The absorbing mechanism of the proposed structure is elucidated through power density plot and electric field analysis at 8 GHz as presented in Fig. 3 (E and F). At this incident frequency, the absorption shifts from 98.9 to 78.1% and transmission from 1.1 to 20.8% when the structure transforms from the collapsed (70°) to the expanded form (30°). As the range of the antenna is proportional to the square root of the transmitted power according to Friis transmission equation (*39*), this transmission change from 1.1 to 20.8% translates to change of range from 10.48 to 44.72% of the original

detectable range. This increased range in the expanded form enables the transmission of signal to further a receiver in transmission mode and detect an object further away through the internal radar.

The power density plot in Fig. 3E highlights the varying location of the attenuation area. While connectors and hinges have little impact on the attenuation, as these components are made from polymers that transmit incoming waves with nearly zero dielectric loss tangent (0.03), the crisscross trusses made from the dielectric lossy material (CB/PLA) with a high dielectric loss tangent (1.35) govern the attenuation (*14*). In the collapsed form (70°), areas highlighted in red that indicate strong attenuation are concentrated in sharp corners and edges of the upper half the trusses. Because of the impedance mismatch between a lossy material and free space from the difference in permittivity, incoming waves are partially reflected and scattered when entering surfaces or corners of the truss. If the structure were composed only of a 2D planar design, without angled and intertwined trusses—such as a solid box as presented in a previous study (*14*)—then the collapsed form would have a limited absorption capacity due to the impedance mismatch. However, owing to the closely packed and interlinked trusses, reflected waves from a single truss are again absorbed by neighboring trusses, leading to increased attenuation in the collapsed form. However, as the gaps between trusses increase with the structure expanded, the dissipation area highlighted in red also diminishes as this interaction between trusses gradually disappears, leading to limited attenuation from reflected and scattered waves. The 3D isosurface electric field plot in Fig. 3F supports this explanation, where the electric field interacts most strongly with the intertwined trusses in the collapsed form (70°), with little electric field formed below the structure. Meanwhile, as the structure expands with rotation, the reduced interaction between structure and electromagnetic wave allows the waves to transmit through the structure, leading to increased transmission at 30°.

Fabrication and assembly of the tunable structure for experimental verification

The optimized tunable structure for broadband absorption and transmission is manufactured and tested to validate three main objectives. First, we establish the fabrication and assembly method for a modular unit cell design, where the total area covered by the structure can be adjusted based on application requirements. Second, it experimentally validates the optimized structure obtained from the data-driven design through free-space electromagnetic response measurement. Third, the assembled structure demonstrates the synchronized actuation of the tunable structures from mechanical inputs.

Figure 4A shows the fully assembled tunable structure collapsed in 70° angle with the dimension configured in Fig. 3A. Because of its rectangular and circular periodicity of the interlinked trusses, the entire structure can be fabricated and assembled using only three components: truss, connector, and hinge. The truss is fabricated using fused filament fabrication (FFF) with a CB/PLA composite filament. Connectors are fabricated using PolyJet, a multimaterial jetting additive manufacturing process, to seamlessly create flexible and rigid parts in a single print with TangoBlack Plus, a rubber-like material, and VeroWhite, a rigid photopolymer. This multimaterial connector enables snap-on assembly of the revolute joint of the truss structure while providing enough stiffness to facilitate the rotation of the revolute joint between connectors and the truss. While using a single additive manufacturing apparatus with PolyJet is advantageous in terms of reducing the number of fabrication process and achieving higher printing resolution, FFF is used as it provides the option of a dielectric lossy material (CB/PLA). Polycarbonate mechanical screws (2.5 mm in diameter) are used for the hinge part that connects two trusses together with a revolute joint in the middle. Detailed design, fabrication, and assembly procedures are further described in Materials and Methods and fig. S2.

The experimental measurement of the electromagnetic response of the tunable structure in the microwave range is characterized through a bistatic free-space measurement system. To meet the minimum sample size required for the experiment, a total of 16 identical crisscross unit cell structures are assembled in a 4–by–4 array. The advantage of snap-on assembly is that the size of the tunable absorber is adjustable based on the coverage area requirement (Fig. 4B). A larger area to be covered by the absorber can be achieved by simply attaching more unit cell structures to the existing arrays. A schematic in Fig. 4C describes the experimental setup of the bistatic antenna, where the tunable structure is positioned at the center between spot-focused antennas with mechanical clamps. To accurately position the trusses at the exact rotational angle, an acrylic jig outside the measured area is used to locate the connectors in the exact position as depicted in Fig. 4D. The spacing between connectors in the acrylic jig is calculated with Eq. 1, where $S_{connectors}$ is the spacing between connectors, l_{joint} is the length from the center to the revolute joint in the connector, l_{truss} is the truss length, and θ is the rotational angle. Detailed jig design and dimensions for spacing calculation are provided in fig. S3. Figure 4E presents the tunable structure positioned at varying angles from collapsed to expanded mode.

$$S_{connectors} = 2 \times l_{joint} + l_{truss}\cos(\theta) \quad (1)$$

Scattering parameters are measured from 5.85 to 18 GHz by changing the rotational angle to five different positions (30°, 40°, 50°, 60°, and 70°). The plotted solid lines in Fig. 4 (F and G) represent the measured absorptions and transmissions from the bistatic free-space measurement, with each line consisting of 1470 data points at an average step size of 0.008 GHz. The tunable structure at 70° achieves broadband absorption with a minimum of 95.3%, an average absorption of 98.1%, and a nearly perfect absorption of 99.7% at 18.0 GHz (Fig. 4F). This broadband absorption coverage can also be described with the criterion of relative tuning range (W_{RTR}) value of 101.9% with a range from 5.85 to 18 GHz. W_{RTR} is a criterion used to compare the operating frequency range of absorbers, calculated by Eq. 2. In this equation, f_{max}, f_{min}, and f_{center} is the maximum, minimum, and center frequencies at which the absorber achieves 90% absorption. Here, f_{center} equals $(f_{max} + f_{min})/2$.

$$W_{RTR} = \frac{(f_{max} - f_{min})}{f_{center}} \quad (2)$$

The experiment aligns with the FEA results plotted in the dashed line, validating the optimization goal of broadband absorption across the entire bandwidth. As the structure expands from 70° to 30°, transmission gradually increases. For instance, at 7.3 GHz, measured transmission shifts from 1.8 to 24.2% when the structure changes from collapsed (70°) to expanded (30°). This difference of more than 20% in transmission can be used for close-range detection of the external environment with an internal antenna or for

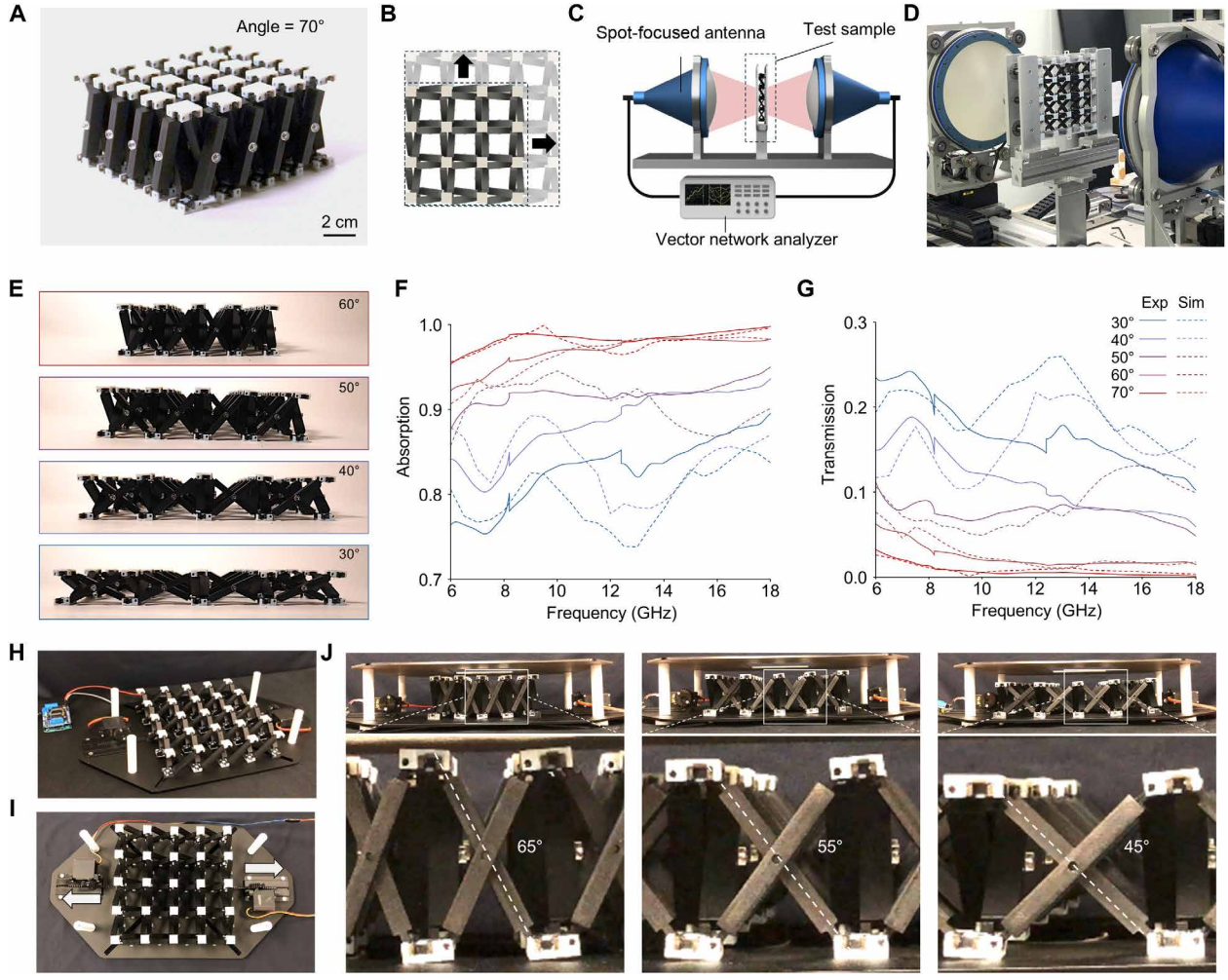

Fig. 4. Fabricated tunable structure and experiment results. (**A**) A photograph of the fabricated and assembled tunable structure positioned in 70°. (**B**) Adjustable coverage area through additionally assembled arrays. (**C**) A schematic representation of the bistatic radar setup for electromagnetic response measurement. (**D**) A photograph of the actual test setup with the structure mounted between the antennas. (**E**) Transformation of the tunable structure with varying angles. Experimental results of (**F**) absorption and (**G**) transmission compared with predicted results. (**H**) Isometric and (**I**) top view of the actuation platform. (**J**) Automated synchronized motion with linear actuators.

data transmission to the outside when in the expanded form. For example, 1.8% transmission can achieve 13.4% of the range of internal antenna, while 24.2% can send the signal to 49.1% of the original range as the range is proportional to the square root of transmitted power (*39*). Once the temporary transmission is done, the structure can quickly switch into stealth mode by changing the angles of the structure into a collapsed form. These results experimentally validate the design objective of the tunable structure achieving a switch from broadband absorption to transmission mode.

While the measured absorption and transmission data at high rotational angles (60° and 70°) match well with the simulated results, the discrepancy between simulated and experimental results increases as the structure expands (30°, 40°, and 50°), and the incident frequency increases (Fig. 4, F and G). Mean absolute errors between experimental and simulated results are less than 1% in both transmission and absorption at 60° and 70° but increase up to 6.3% at 40°, as described in fig. S4. This difference can be explained with difference in the incoming wave between simulation and experimental setups. The simulation setup assumes uniform ideal plane wave entering perpendicular to the structure. However, the experimental setup uses a spot-focused antenna which introduces slight deviation in the incident wave direction (fig. S4) (*40*). When in a collapsed form, since the structure results in an attenuation-dominant response, the impact of angular deviation in the incident wave diminishes. However, as the transmission increases with the expanded form, slight deviations in the incident angle alter the absorption and scattering mechanism of the structure. At lower frequencies, below 9 GHz, the relatively longer wavelength averages out the small deviations, but as the wavelength becomes shorter at higher frequencies, differences between planar and nonplanar waves cause deviations in the electromagnetic response.

Last, a custom platform is designed to demonstrate the synchronized mechanical transformation of the assembled tunable structure (Fig. 4, H to J). As the entire array of interlinked trusses moves

simultaneously, connected through revolute joints in connectors and central hinges, a single mechanical rotation of a revolute joint results in the transformation of the whole structure. Thus, a linear actuator attached to a connector, or a rotational motor attached to the center of truss, leads to a synchronized movement. In the proposed platform, two linear servos, moving in an equal length but toward the opposite direction, are connected to two connectors on the outer edge. While a single actuator can achieve transformation of the structure when the other end is fixed, the platform introduces linear actuation on both connectors at the ends, moving in equal distance so that the origin of the tunable structure is always centered (Fig. 4, H and I). Exact rotational angle of the structure can be controlled through translating the connectors using Eq. 1. The main advantage of this platform is that the electromagnetic response can be adjusted in real time through a microcontroller connected to the motors. For instance, the transformation of the structure from 45°, 55°, to 65° is shown in Fig. 4J, and the real-time transformation is presented in movie S1. While the proposed platform only shifts from 65° to 45° due to the limited strokes of the servos, it validates the synchronized actuation mechanisms. In a real-world environment, the proposed platform can be combined with an existing broadband absorber to enable transmitting capability while maintaining stealth characteristics (fig. S5). A plausible scenario would involve maintaining the collapsed form for stealth functionality by default but shifting to the expanded form only when transmitting signals from the internal antennas.

The competitive advantages of crisscross tunable absorbers proposed in this work compared to state-of-art mechanically tunable electromagnetic wave absorbers are broad operating frequencies, a new function of switching between absorption and transmission, and automated mechanical actuation, as summarized in Table 1. First, by using structural absorption, the chameleon-inspired tunable structure achieves broadband absorption in attenuation mode with a broad operating frequency achieving W_{RTR} of 101.9%. Second, the proposed design demonstrates variable electromagnetic responses between broadband absorption and transmission, compared to conventional tunable structures with limited tunability in controlling reflection loss or peak absorption. This additional transmission mode enables applications such as smart windows transmitting signals only in necessary timing. Last, the crisscross mechanism allows automated control of the entire structure with a single mechanical actuation. While various tuning mechanisms such as mechanical strain (*41*), tailoring thickness (*42*), or origami structures (*25*, *43*, *44*) have been suggested, the actuation of these structures is not thoroughly covered, often requiring manual transformation. As demonstrated with the platform, the transformation of the crisscross structure has major advantages in being automated, real-time, and precise control through mechanical actuation.

DISCUSSION

Inspired by the chameleon's ability to vary visible light reflection through changes in its photonic lattice structure, a previously unidentified crisscross truss structure was introduced in this study to achieve tunable electromagnetic responses with a single unit cell. Rather than a randomly selected design, the data-driven design through a machine learning–trained surrogate model expedited the optimization process for broadband absorption and transformation toward transmission. Compared to other traditional structural tunable absorbers that only focused on demonstrating tunability of reflection loss or absorption, our work offers the ability to switch to transmission mode, a crucial feature required for many applications. The optimized structure was numerically and experimentally validated for its transformation between broadband absorption and transmission. While the range of operating frequencies defined in this study was limited by the measuring antenna setup, the effective bandwidth could be further expanded toward a lower- and higher-frequency range with advanced measurement setups.

In addition, five input parameters were used to explore the electromagnetic response, which was sufficient to demonstrate varying electromagnetic response of broadband absorption more than 90% in the 5.85 to 18 GHz and peak transmission up to 20.8% when

Table 1. Summary of state-of-art mechanically tunable electromagnetic wave absorbers.

Reference	Operating frequencies	W_{RTR} %	Tunable electromagnetic responses	Tuning mechanism	Automated mechanical actuation
(*41*)	1.15–11.56 GHz	3.6%	Shifting peak absorption	Mechanically stretching conductive rubber	No
(*42*)	8.0–8.9 GHz	10.6%	Shifting peak absorption	Tailoring thickness of air gaps	No
(*47*)	5.78–6.96 GHz	18.5%	Shifting peak absorption	Tailoring thickness of air gaps	Automated
(*48*)	5.80–16.2 GHz	94.5%	Broadband absorption to reflection	Tailoring thickness of water layer	No
(*43*)	6.0–16.0 GHz	90.9%	Broadband absorption to reflection	Origami (folding)	No
(*25*)	3.4–18 GHz	136.0%	Broadband absorption bandwidth	Origami (folding)	No
(*44*)	5.0–20 GHz	120.0%	Broadband absorption bandwidth	Origami (folding)	No
This work	5.85–18.0 GHz	101.9%	Broadband absorption to transmission	Crisscross trusses	Automated

expanded. Adding design complexity to the geometry, such as curvature on a truss or multilayered structure, could further enhance the tuning of peak transmission, improving its usability in real-world applications. The manufacturing and assembly of the proposed structures are also presented, with synchronized transformation where the entire system transforms with the actuation platform. Structures connected with unique interlinked crisscross trusses achieve synchronized movement. Further exploration is required on properties beyond electromagnetic response, such as advanced mechanical properties, to develop multifunctional structural absorber in the future. In conclusion, the design methodology and manufacturing of the tunable structural absorber adopted in this work offer a way to control the electromagnetic responses, addressing the tuning of electromagnetic responses beyond reflective loss and covering both broadband absorption and peak transmission.

MATERIALS AND METHODS

FEA of electromagnetic properties

Electromagnetic wave simulation is conducted through the COMSOL Multiphysics RF module to assess the electromagnetic responses of the tunable structure. The structure is constructed assuming an infinite 3D array with Floquet-periodic boundary conditions on four sides, with the tunable structure located between the transmitter and the receiver as described in fig. S6. The unit cell structure is parametrized so that the model can be adjusted with varying truss length, width, thickness, and rotational angle. Permittivity and permeability of CB/PLA are used for the dielectric lossy material–based trusses, and properties of polylactic acid are used for the connector and hinge assuming nonconductive polymer components where the permittivity and permeability are extracted from prior work (*15*). The rest of the volume between the ports is filled with air, and the space outside the ports is set as perfectly matched layers. The incidence angle is set to 0° with TE (transverse electric) polarization. Mesh is generated through the physics-controlled mesh provided from COMSOL which is based on the incident frequency value. From the simulated results, reflection (R), transmission (T), and absorption (A) are calculated from the S parameters: $R = |S_{11}|^2$, $T = |S_{21}|^2$, $A = 1 - R - T$. Further information about the simulation setup and parameters can be found in the Supplementary Materials.

Surrogate model generation and optimization

Considering the parameterized design space, 5000 datasets are generated from randomly generated input variables including truss length, width, thickness, incident frequency, and rotational angle. These datasets are split into an 8:2 ratio for training and test sets, and a neural network is constructed using Keras library with TensorFlow (*45*). The architecture of the neural network model includes three hidden layers, each containing 128 neurons with ReLu activation functions, and an output layer with a sigmoid activation function to produce absorption and transmission values ranging from 0 to 1. The neural network is trained for 2000 epochs. Using the neural network–trained surrogate model, the structure is optimized to fulfill the objective functions. The optimization process using a genetic algorithm involves (*46*): (i) randomly generating 100 candidates, (ii) ranking the top five candidates based on fitness evaluation, (iii) performing crossover and mutation (with a 10% probability) to generate 95 new offsprings, and (iv) combining the top candidates and offsprings to form a new population and repeating the loop until reaching the maximum fitness score or 20 generations. For broadband absorption objectives, the fitness function is evaluated by counting the number of frequency steps (0.1 GHz) that exceeds 90% absorption between 4 and 12 GHz.

Fabrication, assembly, and actuation of the tunable structure

The trusses are manufactured using an FFF 3D printer (Ultimaker S3) with 2.85-mm-diameter CB reinforced polylactic acid filament (Conductive filament, Protopasta). The 3D printing condition is set to 40 mm/s for printing speed, 220°C for nozzle temperature, and 50°C for bed temperature. Each set of crisscross trusses composes of one truss with a clearance hole in the middle and another with an M2.5 thread tapped by to form a revolute joint using M2.5 polycarbonate screws. The connectors are manufactured using the PolyJet 3D printer (Objet350, Stratasys) with a mix of two photopolymer-based materials: VeroWhite (Stratasys) for the rigid part and TangoBlack Plus (Stratasys) for the flexible part. The fabricated components are manually assembled by snapping the truss onto the connector, with the detailed procedure described in fig. S2. To actuate the assembled tunable structure, two servo motors (MG 995, Towerpro) are controlled with an Arduino microcontroller connected with an L293 shield, transforming the rotation into linear actuation using 3D printed gears and linear guides.

Electromagnetic property specification

A spot-focused bistatic antenna (free-space measurement systems, Microwave Measurement System) is used to measure the electromagnetic responses of the fabricated tunable structure. With the sample positioned at the center on a motorized stage, two antennas connected to the vector network analyzer measure scattering parameters for transmission and reflection in decibels. Three bandwidths of 5.85 to 8.2 GHz, 8.2 to 12.4 GHz, and 12.4 to 18.0 GHz are measured for each sample by switching antennas. Two identical acrylic jigs, fabricated with a laser cutter, are used at the top and the bottom of the sample to locate the connecters at the boundaries for precise positioning of the rotational degree. Sample dimensions change by rotating the angle, from 139.0 mm by 139.0 mm by 62.4 mm at 70° to 261.3 mm by 261.3 mm by 36.7 mm at 30°. The acrylic jigs are positioned outside the measurement windows (110 mm by 110 mm) to avoid interfering with the measurement results. TE polarization mode is used for the measurements.

Supplementary Materials

The PDF file includes:

Supplementary Text
Figs. S1 to S6
Tables S1 and S2
Legend for movie S1

Other Supplementary Material for this manuscript includes the following:

Movie S1

REFERENCES AND NOTES

1. X. Sun, M. Yang, S. Yang, S. Wang, W. Yin, R. Che, Y. Li, Ultrabroad band microwave absorption of carbonized waxberry with hierarchical structure. *Small* **15**, e1902974 (2019).
2. H. Lv, Z. Yang, P. L. Wang, G. Ji, J. Song, L. Zheng, H. Zeng, Z. J. Xu, A voltage-boosting strategy enabling a low-frequency, flexible electromagnetic wave absorption device. *Adv. Mater.* **30**, 1706343 (2018).

3. X. Zhang, X. Tian, N. Wu, S. Zhao, Y. Qin, F. Pan, S. Yue, X. Ma, J. Qiao, W. Xu, W. Liu, J. Liu, M. Zhao, K. K. Ostrikov, Z. Zeng, Metal-organic frameworks with fine-tuned interlayer spacing for microwave absorption. *Sci. Adv.* **10**, eadl6498 (2024).
4. Z.-L. Hou, X. Gao, J. Zhang, G. Wang, A perspective on impedance matching and resonance absorption mechanism for electromagnetic wave absorbing. *Carbon* **222**, 118935 (2024).
5. F. Qin, C. Brosseau, A review and analysis of microwave absorption in polymer composites filled with carbonaceous particles. *J. Appl. Phys.* **111**, 061301 (2012).
6. A. Iqbal, F. Shahzad, K. Hantanasirisakul, M.-K. Kim, J. Kwon, J. Hong, H. Kim, D. Kim, Y. Gogotsi, C. M. Koo, Anomalous absorption of electromagnetic waves by 2D transition metal carbonitride Ti3CNT x (MXene). *Science* **369**, 446–450 (2020).
7. T. Xia, C. Zhang, N. A. Oyler, X. Chen, Hydrogenated TiO_2 nanocrystals: A novel microwave absorbing material. *Adv. Mater.* **25**, 6905–6910 (2013).
8. B.-X. Wang, C. Xu, G. Duan, W. Xu, F. Pi, Review of broadband metamaterial absorbers: From principles, design strategies, and tunable properties to functional applications. *Adv. Funct. Mater.* **33**, 2213818 (2023).
9. P. Yu, L. V. Besteiro, Y. Huang, J. Wu, L. Fu, H. H. Tan, C. Jagadish, G. P. Wiederrecht, A. O. Govorov, Z. Wang, Broadband metamaterial absorbers. *Adv. Opt. Mater.* **7**, 1800995 (2019).
10. C. M. Watts, X. Liu, W. J. Padilla, Metamaterial electromagnetic wave absorbers. *Adv. Mater.* **24**, OP98-OP120 (2012).
11. L. Yin, J. Doyhamboure, X. Tian, D. Li, Design and characterization of radar absorbing structure based on gradient-refractive-index metamaterials. *Compos. B Eng.* **132**, 178–187 (2018).
12. W.-H. Choi, C.-G. Kim, Broadband microwave-absorbing honeycomb structure with novel design concept. *Compos. B Eng.* **83**, 14–20 (2015).
13. J. Lee, D. D. Lim, J. Park, J. Lee, D. Noh, G. X. Gu, W. Choi, Multifunctionality of additively manufactured Kelvin foam for electromagnetic wave absorption and load bearing. *Small* **19**, 2305005 (2023).
14. D. D. Lim, S. Lee, J.-H. Lee, W. Choi, G. X. Gu, Mechanical metamaterials as broadband electromagnetic wave absorbers: Investigating relationships between geometrical parameters and electromagnetic response. *Mater. Horiz.* **11**, 2506–2516 (2024).
15. D. D. Lim, J. Park, J. Lee, D. Noh, J. Lee, J. Choi, W. Choi, Broadband mechanical metamaterial absorber enabled by fused filament fabrication 3D printing. *Addit. Manuf.* **55**, 102856 (2022).
16. Q. An, D. Li, W. Liao, T. Liu, D. Joralmon, X. Li, J. Zhao, A novel ultra-wideband electromagnetic-wave-absorbing metastructure inspired by bionic gyroid structures. *Adv. Mater.* **35**, 2300659 (2023).
17. L. Yin, X. Tian, Z. Shang, D. Li, Ultra-broadband metamaterial absorber with graphene composites fabricated by 3D printing. *Mater. Lett.* **239**, 132–135 (2019).
18. P. Gong, L. Hao, Y. Li, Z. Li, W. Xiong, 3D-printed carbon fiber/polyamide-based flexible honeycomb structural absorber for multifunctional broadband microwave absorption. *Carbon* **185**, 272–281 (2021).
19. Y. Duan, Q. Liang, Z. Yang, Z. Li, H. Yin, Y. Cao, D. Li, A wide-angle broadband electromagnetic absorbing metastructure using 3D printing technology. *Mater. Des.* **208**, 109900 (2021).
20. G. Zhang, H. Wang, W. Xie, S. Zhou, Z. Nie, G. Niwamanya, Z. Zhao, H. Duan, Advancements in 3D-printed architectures for electromagnetic interference shields. *J. Mater. Chem. A* **12**, 5581–5605 (2024).
21. C. Sun, D. Li, T. Liu, Q. An, C. Zhang, Y. Li, W. Liao, Design of functionally gradient metastructure with ultra-broadband and strong absorption. *Compos. B Eng.* **280**, 111484 (2024).
22. W. Li, M. Xu, H. X. Xu, X. Wang, W. Huang, Metamaterial absorbers: From tunable surface to structural transformation. *Adv. Mater.* **34**, 2202509 (2022).
23. Y. Zhang, L. Miao, S. Guo, Z. Huang, Z. Cao, Y. He, J. Wei, C. Li, J. Jiang, A broadband tunable frequency selective surface absorber for oblique incidence applications. *J. Phys. D Appl. Phys.* **53**, 055105 (2019).
24. Z. Yin, Y. Lu, T. Xia, W. Lai, J. Yang, H. Lu, G. Deng, Electrically tunable terahertz dual-band metamaterial absorber based on a liquid crystal. *RSC Adv.* **8**, 4197–4203 (2018).
25. X. Chen, W. Li, Z. Wu, Z. Zhang, Y. Zou, Origami-based microwave absorber with a reconfigurable bandwidth. *Opt. Lett.* **46**, 1349–1352 (2021).
26. J. Teyssier, S. V. Saenko, D. van der Marel, M. C. Milinkovitch, Photonic crystals cause active colour change in chameleons. *Nat. Commun.* **6**, 6368 (2015).
27. N. Reyes, F. Casado, V. Tapia, C. Jarufe, R. Finger, L. Bronfman, Complex dielectric permittivity of engineering and 3D-printing polymers at Q-band. *J. Infrared Millim. Terahertz Waves* **39**, 1140–1147 (2018).
28. A. Al Takach, F. M. Moukanda, F. Ndagijimana, M. Al-Husseini, J. Jomaah, Two-line technique for dielectric material characterization with application in 3D-printing filament electrical parameters extraction. *Prog. Electromagn. Res. M* **85**, 195–207 (2019).
29. L. M. Mäthger, R. T. Hanlon, Malleable skin coloration in cephalopods: Selective reflectance, transmission and absorbance of light by chromatophores and iridophores. *Cell Tissue Res.* **329**, 179–186 (2007).
30. B. Zheng, Z. Zheng, G. X. Gu, Designing mechanically tough graphene oxide materials using deep reinforcement learning. *NPJ Comput. Mater.* **8**, 225 (2022).
31. W. Xi, Y.-J. Lee, S. Yu, Z. Chen, J. Shiomi, S.-K. Kim, R. Hu, Ultrahigh-efficient material informatics inverse design of thermal metamaterials for visible-infrared-compatible camouflage. *Nat. Commun.* **14**, 4694 (2023).
32. S. Yu, P. Zhou, W. Xi, Z. Chen, Y. Deng, X. Luo, W. Li, J. Shiomi, R. Hu, General deep learning framework for emissivity engineering. *Light Sci. Appl.* **12**, 291 (2023).
33. Y. Kim, C. Yang, Y. Kim, G. X. Gu, S. Ryu, Designing an adhesive pillar shape with deep learning-based optimization. *ACS Appl. Mater. Interfaces* **12**, 24458–24465 (2020).
34. S. Yu, J.-S. Yu, Z. Chen, Q. Li, Z. Wang, X. Luo, S.-K. Kim, R. Hu, Ultrahigh visible-transparency, submicrometer, and polymer-free radiative cooling meta-glass coating for building energy saving. *ACS Photonics* **11**, 3412–3423 (2024).
35. S. Lee, Z. Zhang, G. X. Gu, Generative machine learning algorithm for lattice structures with superior mechanical properties. *Mater. Horiz.* **9**, 952–960 (2022).
36. S. Luan, E. Chen, J. John, S. Gaitanaros, A data-driven framework for structure-property correlation in ordered and disordered cellular metamaterials. *Sci. Adv.* **9**, eadi1453 (2023).
37. R. Hu, S. Iwamoto, L. Feng, S. Ju, S. Hu, M. Ohnishi, N. Nagai, K. Hirakawa, J. Shiomi, Machine-learning-optimized aperiodic superlattice minimizes coherent phonon heat conduction. *Phys. Rev. X* **10**, 021050 (2020).
38. S. Lee, Z. Zhang, G. X. Gu, Deep learning accelerated design of mechanically efficient architected materials. *ACS Appl. Mater. Interfaces* **15**, 22543–22552 (2023).
39. H. T. Friis, A note on a simple transmission formula. *Proc. IRE* **34**, 254–256 (1946).
40. D. Wu, Z. Feng, X. Zhuang, in *2015 IEEE International Wireless Symposium (IWS 2015)* (IEEE, 2015), pp. 1-4.
41. F. Zhang, S. Feng, K. Qiu, Z. Liu, Y. Fan, W. Zhang, Q. Zhao, J. Zhou, Mechanically stretchable and tunable metamaterial absorber. *Appl. Phys. Lett.* **106**, 103903 (2015).
42. H. Jeong, M. M. Tentzeris, S. Lim, Frequency-tunable electromagnetic absorber by mechanically controlling substrate thickness. *Int. J. Antennas Propag.* **2018**, 1963051 (2018).
43. T.-L. Pham, K. B. Xuan, B. S. Tung, L. D. Hai, L. Van Long, V. D. Lam, N. T. Tung, Origami-based stretchable bi-functional metamaterials: Reflector and broadband absorber. *J. Phys. D Appl. Phys.* **54**, 165111 (2021).
44. Z. Zhu, Y. Li, Z. Qin, L. Jiang, W. Wang, H. Chen, J. Wang, L. Zheng, S. Qu, Miura-ori based reconfigurable multilayer absorber for high-efficiency wide-angle absorption. *Opt. Express* **32**, 24091–24106 (2024).
45. F. Chollet *et al*., Keras. Available at: https://github.com/keras-team/keras (2015).
46. Z. Jin, D. D. Lim, X. Zhao, M. Mamunuru, S. Roham, G. X. Gu, Machine learning enabled optimization of showerhead design for semiconductor deposition process. *J. Intell. Manuf.* **35**, 925–935 (2024).
47. J. Kim, H. Jeong, S. Lim, Mechanically actuated frequency reconfigurable metamaterial absorber. *Sens. Actuators A Phys.* **299**, 111619 (2019).
48. Y. Zhang, H. Dong, N. Mou, H. Li, X. Yao, L. Zhang, Tunable and transparent broadband metamaterial absorber with water-based substrate for optical window applications. *Nanoscale* **13**, 7831–7837 (2021).

Acknowledgments

Funding: This research was supported by the Bakar Foundation, Alfred P. Sloan Foundation, the National Science Foundation Extreme Science and Engineering Discovery Environment (XSEDE) Bridges system (fund number: ACI-1548562), and the University of California, Berkeley Molecular Graphics and Computation Facility (fund number: NIH S10OD034382). **Author contributions:** Conceptualization: D.D.L. and G.X.G. Methodology: D.D.L., A.I., J.L., J.J., W.C., and G.X.G. Investigation: D.D.L., W.C., and G.X.G. Formal analysis: D.D.L., J.L., A.I., and J.J. Visualization: D.D.L. and J.J. Validation: D.D.L., A.I., and J.L. Writing—original draft: D.D.L. Writing—review and editing: A.I., J.L., J.J., G.X.G., and W.C. Supervision: W.C. and G.X.G. **Competing interests:** The authors declare that they have no competing interests. **Data and materials availability:** All data needed to evaluate the conclusions in the paper are present in the paper and/or the Supplementary Materials.

Submitted 21 August 2024
Accepted 11 December 2024
Published 15 January 2025
10.1126/sciadv.ads3499